



Deformation in the lowermost mantle: From polycrystal plasticity to seismic anisotropy

Hans-Rudolf Wenk^{a,*}, Sanne Cottaar^a, Carlos N. Tomé^b, Allen McNamara^c, Barbara Romanowicz^{a,d}

^a Department of Earth and Planetary Science, University of California, Berkeley, CA 94720, United States

^b MST-8, Los Alamos National Laboratory, Los Alamos, NM 87545, United States

^c School of Earth and Space Exploration, Arizona State University, Tempe, AZ 85287, United States

^d Berkeley Seismological Laboratory, University of California, Berkeley, CA 94720, United States

ARTICLE INFO

Article history:

Received 11 October 2010

Received in revised form 10 March 2011

Accepted 12 March 2011

Available online 16 April 2011

Editor: P. Shearer

Keywords:

D'' anisotropy
texture development
post-perovskite
perovskite
magnesiowuestite
lowermost mantle

ABSTRACT

In the deep earth, deformation occurs at many scales: large-scale convection produces subduction of slabs and upwelling of plumes in the mantle. At the high temperature/high pressure conditions, strain is accommodated through crystal plasticity, either by diffusion or the movement of dislocations. Slip causes crystal rotations and thus produces a characteristic pattern of crystal preferred orientation and corresponding anisotropy of physical properties at the macroscopic scale. In this study we use polycrystal plasticity, with experimentally derived deformation mechanisms for perovskite, post-perovskite and magnesiowuestite, to predict texture development along streamlines in a 2D geodynamic convection model of the lowermost mantle. Strong preferred orientation develops during subduction and upwelling, while during spreading along the core–mantle boundary the orientation pattern is relatively stable. From preferred crystal orientation and single crystal elastic properties, bulk elastic properties can be calculated and compared with seismic observations. Post-perovskite with predominant (001) slip and magnesiowuestite with {110} and {111} slip produce anisotropy patterns which are consistent with observed anisotropy, i.e. fast S-waves polarized parallel to the core–mantle boundary and anti-correlation between P and S-wave anisotropies. In contrast, perovskite with dominant (001) slip and two post-perovskite models with dominant slip on (010) and (100) produce anisotropy patterns which are inconsistent with seismic observations.

© 2011 Elsevier B.V. All rights reserved.

1. Introduction

Geodynamic convection models of the Earth predict large strains, particularly during subduction of slabs and upwelling of plumes. In the solid Earth, these strains are accommodated at the microscopic scale by dislocation movements, intracrystalline diffusion and grain boundary diffusion. If dislocations are mobile, crystals rotate, attain preferred orientation and this is expressed by elastic anisotropy at the macroscopic scale. Development of anisotropy during convection has been modeled in the upper mantle (Becker et al., 2008; Blackman et al., 2002; Dawson and Wenk, 2000; Kaminski and Ribe, 2004), the lower mantle (Wenk et al., 2006a) and the inner core (Buffett and Wenk, 2001; Wenk et al., 2000). Here we investigate the lowermost mantle, composed mainly of perovskite, post-perovskite and magnesiowuestite. We will use a geodynamic model to define the macroscopic deformation in a convecting mantle and then apply polycrystal plasticity calculations to infer orientation changes of crystals as they advance along streamlines. Calculations are done for

various combinations of mineral phases and slip systems. The orientation patterns are then used to calculate the elastic tensor at different locations in D'' by averaging single crystal elastic properties over the orientation distribution and infer anisotropy of seismic waves.

The region just above the core–mantle boundary has fascinated seismologists for a long time. It was Bullen (1950) who gave it the name D'' to distinguish it from the rest of the lower mantle, because of the change in seismic velocity gradient with depth across this region. More recent seismic observations indicate strong lateral and vertical heterogeneities, reflecting the complexity of the thermo-chemical boundary layer (Helmberger et al., 2005; Houser, 2007). Experimental (Hunt et al., 2009) and theoretical (Ammann et al., 2010) investigations suggest that D'' is weaker than the overlying mantle and thus deformation may be localized. While the lower mantle is thought to be largely isotropic, there is evidence for seismic anisotropy in D'' (e.g. Lay et al., 1998a; Vinnik et al., 1989). The cause for anisotropy at the base of the mantle is uncertain. If the large strains that are attained during convection are at least partially accommodated by dislocation creep, it is expected to produce seismic anisotropy due to the alignment of anisotropic minerals (e.g., Karato, 1998a,b; Kendall, 2000; Lay et al., 1998a, 1998b). Another possibility is shape-preferred

* Corresponding author.

E-mail address: wenk@berkeley.edu (H.-R. Wenk).

orientation (SPO), alignment of melt inclusions or laminated solid materials (Williams and Garnero, 1996). In this study, we concentrate on lattice preferred orientation (LPO) as a possible cause for anisotropy in the deep mantle. We will also use the word “texture” as synonym to LPO.

Seismologists are restricted in their characterization of anisotropy in the lowermost mantle, because sampling of D'' by sensitive seismic waves is still poor, and in particular the azimuthal coverage is insufficient to distinguish between vertical transverse isotropy (VTI) and other types of anisotropy. Determination of azimuthal anisotropy requires full waveform modeling (e.g. Garnero et al., 2004; Maupin, 1994 and Maupin et al., 2005). Another challenge is to correct for contamination by near-source and near-receiver anisotropy. For this, one approach is to work with deep earthquakes. However, large deep earthquakes are few and their global distribution is limited to South America and the western Pacific.

Nevertheless, global studies show horizontally polarized S-waves travel faster than vertically polarized ones ($V_{SH} > V_{SV}$) in most regions of D'' (e.g. Kustowski et al., 2008; Panning and Romanowicz, 2006). Only beneath the so-called large low shear velocity provinces (LLSVPs), weaker opposite anisotropy can be found (Fig. 1). Regional studies are fairly consistent with the big picture, especially in the Caribbean and under Alaska, although they show that there is smaller scale complexity, especially in the central Pacific (see overview in Wookey and Kendall, 2007). Recently, the use of ScS phases in local studies and correction of the source- and receiver side anisotropy using S-waves has improved, making it possible to measure tilted transverse isotropy (Nowacki et al., 2010; Wookey and Kendall, 2008). Also, almost vertically propagating SKS and SKKS phases have been used to reveal small-scale variations in anisotropy (Long, 2009). Other seismic complexities in the D'' include horizontal velocity discontinuities (Lay, 2008; Lay and Helmberger, 1983; Wyession et al., 1998), sharp vertical boundaries (e.g. Ni et al., 2002; To et al., 2005) and ultra-low velocity zones (e.g. Garnero et al., 1998; Lay et al., 1998b). Furthermore, there appears to be an anti-correlation between P and S wave velocities and anisotropies (e.g. Beghein et al., 2006; Masters et al., 2000; Su and Dziewonski, 1997).

It is important to note that seismic wavelengths in the D'' are on the order of 200 km, averaging any structure over this scale. In this study we aim to link microscopic processes to these macroscopic observations. The approach relies on theories and models developed in materials science. We thought it would be useful to first briefly review and explain some of the background in this presentation, directed at geophysicists and particularly seismologists, to help appreciate that polycrystal deformation is based on straightforward physical principles, but implementation in low-symmetry aggregates is complex and cannot be captured with intuitive estimates or upper/lower bound approximations.

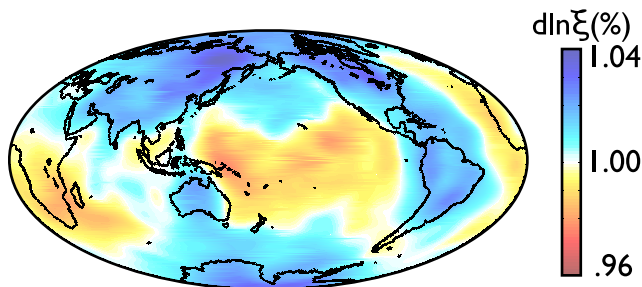


Fig. 1. S-wave anisotropy in D'' at 2800 km depth, illustrated by variations in $\xi = (V_{SH}^2/V_{SV}^2)$, assuming transverse isotropy (Panning and Romanowicz, 2006). Values greater than 1.0 indicate that the fast S-wave is polarized parallel to the CMB and in regions with values less than 1.0 it is perpendicular.

For example, there are statements such as “(100) lattice planes are aligned” or “10% of the crystals are aligned”. In fact, in any deformed aggregate all crystals are oriented in a continuous three-dimensional statistical orientation distribution. It is not the case that one fraction is perfectly parallel and one fraction is random. It is also claimed, on theoretical or experimental evidence, that one slip system is replaced by another one as pressure or temperature changes. The fact is that in each crystal many slip systems must be active for ductile deformation of a polycrystal to take place, even if some of them may be easier to activate under certain conditions. Appropriate references will be provided for those interested in more details. In two appendices we introduce background of polycrystal plasticity and review principles of deformation mechanisms.

2. Geodynamics

The solid state convection in the deep Earth is best assessed with geodynamic models. To investigate the development of convection-induced deformation in the lowermost mantle, we performed 2-dimensional (2D) convection calculations that include slab-like downwellings that descend upon the core–mantle boundary (McNamara et al., 2002, 2003; Lassak, et al., 2007). The calculations are performed by solving the non-dimensional equations for the conservation of mass, momentum, and energy using the Boussinesq approximation. We use a Rayleigh number of 10^7 , referenced to upper mantle viscosity at a non-dimensional temperature of $T = 0.5$.

The viscosity η is a function of temperature, depth, and composition, and includes a viscosity increase at the base of the transition zone (at 660 km depth):

$$\eta(T, z) = \eta_z(z) \exp[A(0.5 - T)] \quad (1)$$

where η_z and z are non-dimensional viscosity and dimensional depth, respectively. $\eta_z(z) = 1$ and 50 for the upper and lower mantles, respectively (e.g., Lithgow-Bertelloni and Gurnis, 1997). A is the activation parameter and T is the non-dimensional temperature. $A = 9.2103$ leads to a viscosity range of 10^4 due to the temperature difference between the hottest and coldest regions of the model.

The conservation equations are solved using our modified version of the convection code Citcom (Moresi and Gurnis, 1996). Temperature boundary conditions are isothermal on the top and bottom, and insulating on the sides. Velocity boundary conditions are free-slip on all boundaries. Before deformation tracers are incorporated, the calculation is run for a sufficient amount of time to reach thermal equilibrium. A snapshot of the temperature field is shown in Fig. 2 (top) and the time evolution is captured in a movie (movie 1 in supplementary material). Resolution tests were performed at both higher and lower resolutions to ensure that the deformation field is adequately resolved and numerically stable.

Internal deformation is tracked using Lagrangian tracers (McNamara et al., 2002, 2003; Merkel et al., 2007; Wenk et al., 2006a). They are introduced as subducted material enters the D'' zone, i.e. 300 km above the core–mantle boundary (CMB). We selected 8 tracers, which are shown in the enlarged segment (Fig. 2 bottom). Note that x is parallel to the CMB and z is in the radial direction. For each tracer, the velocity gradient tensor, L , is stored for each convection time step.

$$L = \begin{pmatrix} \frac{\partial v_x}{\partial x} & \frac{\partial v_x}{\partial z} \\ \frac{\partial v_z}{\partial x} & \frac{\partial v_z}{\partial z} \end{pmatrix} \quad (2)$$

In two dimensions, material deforms by plane strain, i.e. there is no deformation perpendicular to the plane of the picture (Fig. 2). In plane strain there are two special cases, coaxial deformation (pure shear) and non-coaxial deformation (simple shear). We can evaluate this by

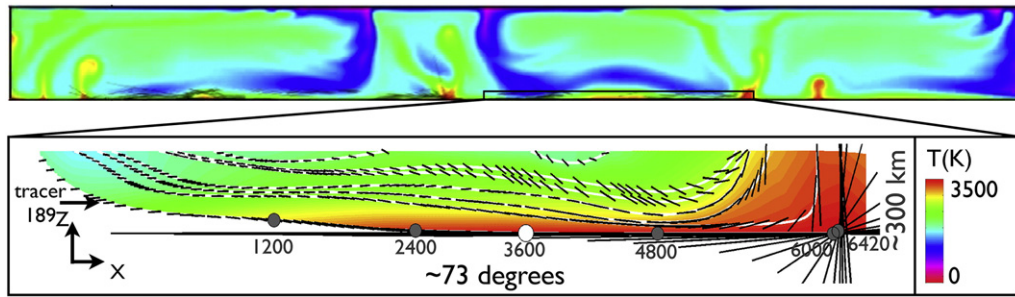


Fig. 2. Geodynamic model for convection in the lower mantle. Top: Snapshot in time on which the cell of interest in this study is outlined. Bottom: Cell of D'' with eight tracers and their respective long strain ellipsoid axes at selected steps. Note that vertical scale is exaggerated. Colors indicate temperature. Circles refer to positions along streamline #189 that have been investigated in detail.

looking at the components of the velocity gradient tensor. In the case of plane strain there are 4 non-zero components $L_{xx} = dV_x/dx$, $L_{xz} = dV_x/dz$, $L_{zx} = dV_z/dx$ and $L_{zz} = dV_z/dz$. The value of these components is plotted as function of time step in Fig. 3. In 2D L_{xx} and L_{zz} are complementary, because we assume no volume change and the trace of \mathbf{L} is zero. The switch in sign plays an important role when distinguishing deformation regimes. Interestingly the vertical shear L_{zx} is very small, except at the very end, during upwelling. L_{xz} is moderate through most of the deformation, suggesting that pure shear dominates. Note that about at one third of its path, the streamline bulges slightly upwards. This is due to development of a large plume that will later divide the cell and eventually cause heterogeneous turnover (Fig. 2 top). But for the time interval of our study, about 2 Gy, the system is remarkably stable. In Fig. 2 (bottom) tracer lines are white and at regular intervals black lines illustrate length and orientation of the long axis of the strain ellipse. For all the lower streamlines there is a clear rotation as the tracer starts upwelling. Temperatures in this D'' model range from about 1500 to 3500 K.

In this paper we follow tracer #189 that progresses closest to the CMB (Fig. 2 bottom). It records parameters in 6420 convection time steps, accumulating a Von Mises strain of 6.4. As is evident from the length of ellipse axes it accumulates the largest strain of all the tracers. Around step 5690 the flow reverses from subduction to upwelling and this causes some large changes, especially for L_{xz} that may be due to numerical instability (Fig. 3).

3. Polycrystal plasticity

Deformation of a polycrystal is a complex process. There are different deformation modes: elastic deformation by lattice distortion, brittle deformation by fracturing, slip by dislocation glide, mechanical twinning, diffusion, the latter expressed by dislocation climb, grain

boundary sliding or recrystallization. Even if only dislocation glide is considered, a polycrystal with many different crystal orientations deforms heterogeneously at the microscopic scale, in order to satisfy compatibility across grain boundaries and maintain stress equilibrium. This feature is best captured with finite element models but because of the enormous computational efforts there are only few applications (e.g. Mika and Dawson, 1999). The most common approach in materials science is with models that keep each grain homogeneous and deform it relative to a matrix of neighbors, imposing various degrees of strain compatibility (upper bound Taylor model) and stress equilibrium (lower bound Sachs model).

For the large strain associated with convection we use a self-consistent visco-plastic polycrystal approach that does not account for elastic deformation, since the latter is negligibly small and does not affect the plastic component. Polycrystal models have several common features: within a polycrystal model the material is represented as an ensemble of crystal orientations (grains) with weights (volume fractions), chosen to represent the initial texture of the aggregate. In this work we use a so-called “Effective Medium” (EM) model, where each grain is treated as an ellipsoidal inclusion embedded in, and interacting with, the EM that represents the polycrystal. The constitutive laws that describe the response of each inclusion and of the medium are visco-plastic, i.e. intermediate between a Newtonian fluid and a rigid solid. The viscoplasticity is described by the stress exponent n of the strain rate $\dot{\epsilon}$ ($\dot{\epsilon} \sim \sigma^n$) which ranges between 0 and ∞ . The effective properties of the medium are not known in advance, and follow from enforcing a condition of consistency with the average of the grains' responses. For this reason EM models are also referred to as self-consistent.

An obvious advantage of polycrystal models is that they explicitly account for anisotropic response because they express the aggregate properties as average over the distribution of crystal orientations. In addition, the advantage of self-consistent polycrystal models is that

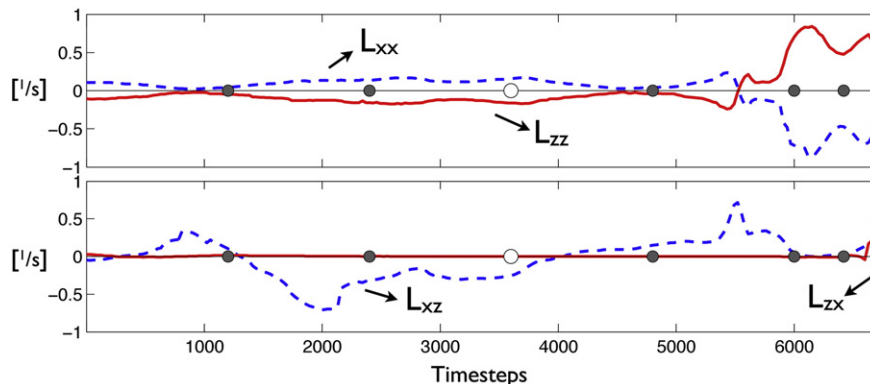


Fig. 3. Evolution of velocity gradient tensor components along tracer #189. Top figure: dashed line is dV_x/dx , solid line is dV_z/dz . Bottom figure: dashed line is dV_x/dz , solid line is dV_z/dx .

they account for the relative anisotropy of grain and medium, as well as grain morphology effects (via the ellipsoidal shape). As a consequence, more deformation is accommodated by those grains favorably oriented, both crystallographically and morphologically, and less by grains unfavorably oriented to activate the soft systems.

In Appendix A (electronic supplement) we describe some details of the visco-plastic self consistent (VPSC) model used (Lebensohn and Tomé, 1993; Lebensohn et al., 2007; Molinari et al., 1987).

To set-up a VPSC calculation, a set of crystal orientations is needed, either randomly generated, or with a preferred orientation pattern if the material is initially textured. In this study no initial texturing is assumed at the top of the D". Each orientation is described by 3 Euler angles defining the relation between sample (i.e. the convection reference system) and crystal coordinate systems. There may be one or several phases in the polycrystalline sample, each with characteristic deformation systems and strength.

A crystal symmetry and a volume fraction are assigned to these phases. Potential slip systems, defined by slip plane and slip direction $\{hkl\} \langle uvw \rangle$, strain rate sensitivity and critical resolved shear stress (crss) as well as hardening coefficients, are specified. This will be described in more detail in the next section. We consider the following phases: perovskite, post-perovskite and periclase/magnesiowuestite. Enforcement of the velocity gradient (Eq. (2)) during successive time intervals describes the macroscopic deformation as a history of incremental strains. Note that even though the macroscopic deformation is in plane strain (2D), polycrystal plasticity is in 3D, i.e. crystal rotations are not confined to the 2D plane of Fig. 2.

The simulations start generally with an equiaxed (spherical) shape of all grains. The grain shape gets updated every step, as explained in Appendix A (electronic supplement), and thus the shapes vary with orientations. In the mantle simulations, with very large strains, extremely distorted ellipsoidal shapes are generated and this is not very realistic. In a dislocation creep regime, at large strains, grains break down into subgrains, first separated by small-angle boundaries and by continuing deformation becoming independent grains. To simulate such a behavior, we stop updating grain shapes once an aspect ratio of 3 has been reached, although we still allow for rigid rotation of the ellipsoid in the plastic flow field. We also assume that half of the deformation is accommodated by slip (dislocation glide) and the other half by diffusion, including grain boundary sliding. Only slip produces orientation changes.

4. Deformation mechanisms

Deformation mechanisms of minerals have been identified mainly through experiments on single crystals and polycrystals. Experimental deformation of rocks and minerals has been pursued for a long time (Pfaff, 1859). It was greatly advanced and the Paterson Volume (Hobbs and Heard, 1986) provides reviews. Since then two major advances have occurred: Paterson and Olgaard (2000) introduced a torsion apparatus that can be used to achieve very large strains. Multi-anvil presses (Wang et al., 2003) allow deformation at conditions of the upper mantle and, more recently, even the transition zone.

However, the lower mantle, that composes most of the volume of the earth, is still out of reach for these conventional instruments. What are the slip systems in silicate perovskite and post-perovskite? One way to obtain information is to use analog phases with similar structures but different chemical compositions, which are stable at lower pressure. Analog systems are problematic, because bonding properties are often different. Another approach is to use first principle calculations to reveal bonding characteristics and infer from them likely slip systems (e.g. Carrez et al., 2007). This is a very powerful new method that is helped by the fact that lower mantle minerals have rather simple crystal structures. A third approach is with unconventional deformation experiments. Diamond anvil cells (DAC), in radial diffraction geometry, not only impose high pressure

but also stress as well and deform aggregates of lower mantle composition at lower mantle pressures (Wenk et al., 2006b). At high pressure, oxides and silicates deform ductily, even at room temperature and during deformation preferred orientation develops. The philosophy is to compare experimental texture patterns with polycrystal plasticity simulations for compression, which assume certain combinations of slip systems. From this 'inverse approach' active slip systems in the DAC experiments can be inferred.

Ductile deformation can occur by a variety of mechanisms and some issues are discussed in Appendix B (electronic supplement). Most significant is dislocation glide, dislocation climb, grain boundary sliding and mechanical twinning. Mechanical twinning can be excluded at the high temperatures and low stresses of the deep mantle, though it may be significant in experiments (Chen et al., 2002; Miyajima and Walte, 2009). Diffusion mechanisms do not produce preferred orientation. Thus we concentrate here on dislocation glide (slip).

Most information is available on MgO (Heidelbach et al., 2003; Lin et al., 2009; Merkel et al., 2002; Tommaseo et al., 2006; Yamazaki and Karato, 2002). The texture that develops in compression experiments at ambient temperature can be described in inverse pole figures (IPF) of the compression direction relative to crystal coordinates. IPFs display crystal symmetry and only the asymmetric unit sector is shown. For MgO there is a maximum at (001) (Fig. 4e). Comparison with VPSC simulations suggests that the dominant slip system consistent with this texture is $\{110\} \langle \bar{1}10 \rangle$, though other systems are also active (Fig. 4j).

Silicate perovskite is the dominant phase in much of the lower mantle. Slip systems have been investigated in analog materials (Poirier et al., 1991), by transmission electron microscopy (Chen et al., 2002) and ab initio simulations (Carrez et al., 2007). Textures produced in DAC experiments (Wenk et al., 2004, Fig. 4d) are compatible with dominant (001) slip along $[100]$, $[001]$ or $\langle 110 \rangle$ (Fig. 4i).

For post-perovskite there is most ambiguity and texture development has been discussed in a series of recent papers. Observed textures are displayed in Fig. 4a–c. Fig. 4a is MgSiO₃ post-perovskite deformed in a DAC (Merkel et al., 2007), Fig. 4b is the structural analog CaIrO₃ deformed in a large volume press (Miyagi et al., 2008), and Fig. 4c is MgSiO₃ post-perovskite deformed in a DAC (Miyagi et al., 2010). These textures are compatible with dominant (100), (010) and (001) slip, respectively (Fig. 4f–h). We will consider all three cases as possibilities and treat them as post-perovskite models A, B and C. We will discuss plausible reasons for the differences later on.

Slip systems that will be used in the mantle polycrystal plasticity simulations, with corresponding normalized critical resolved shear stress coefficients (crss), are listed in Table 1. In this table there are several slip systems for each phase. Those mentioned above are the dominant ones with the lowest crss. Obviously, there is some uncertainty, especially the temperature dependence of crss.

5. Single crystal elastic properties

From orientation patterns obtained by polycrystal plasticity simulations, elastic properties of the aggregate can be obtained by averaging single crystal elastic properties over the orientation distributions of the phases. While it is not possible to determine elastic properties of lower mantle minerals at pressure and temperature experimentally, ab initio calculations of elastic properties are advancing (Wentzcovitch and Stixrude, 2010). For periclase and perovskite there are large changes of single crystal anisotropy with temperature and pressure.

Stackhouse et al. (2005) used ab initio molecular dynamics simulations where the atoms move in real time according to their thermal motion at high temperature and pressure. The elastic constants for post-perovskite were obtained by applying three different orthorhombic and one triclinic type strains, and the induced stresses were averaged along the trajectories. The strength of this

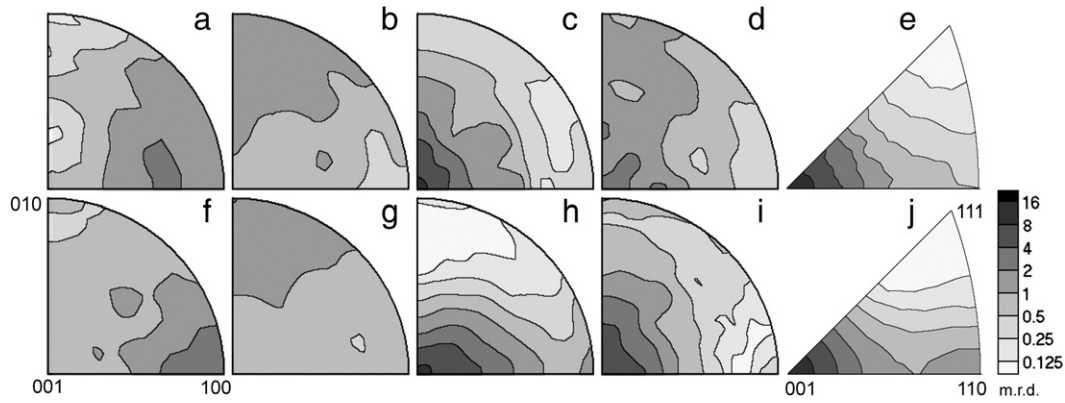


Fig. 4. Compression experiments (a–e) and corresponding polycrystal plasticity simulations to identify slip systems (f–j). Inverse pole figures of the compression direction with crystal coordinates indicated in (f) and (j). (a,f) Model A MgSiO_3 post-perovskite (Merkel et al., 2007), (b,g) model B CaIrO_3 post-perovskite (Miyagi et al., 2008), (c,h) model C MgSiO_3 post-perovskite (Miyagi et al., 2010), (d,i) MgSiO_3 perovskite (Wenk et al., 2004), (e,j) magnesio-wuestite (Lin et al., 2009). Equal area projection, pole densities in multiples of a random distribution (m.r.d.), logarithmic scale.

approach lies in the fact that it includes anharmonic and vibrational effects that are important near melting.

Wentzcovitch et al. (2004, 2006) derived the elastic properties of perovskite and post-perovskite from ab initio perturbation theory where the atoms remain in their equilibrium positions and stress-strain relationships are inferred from the analytic expressions for the second derivative of the energy with respect to atomic displacements (quasiharmonic approximation). An overview of the methods and comparison of results is given in Stackhouse and Brodholt (2007) and Wentzcovitch et al. (2010).

Here we use for MgO stiffness coefficients obtained by Karki et al. (2000), for perovskite values from Wentzcovitch et al. (2004), and for post-perovskite both values of Stackhouse et al. (2005) and of Wentzcovitch et al. (2006). Note that all these calculations were done for pure Mg-endmembers and partial iron substitution was not considered. Iron content does have a significant impact on elasticity of magnesio-wuestite (e.g. Lin et al., 2005) as well as post-perovskite (e.g. Stackhouse and Brodholt, 2008). Table 2 lists stiffness coefficients and densities for the phases at $P = 125$ GPa and $T = 3000$ K, corresponding more or less to step 3600 of tracer #189.

From stiffness coefficients propagation velocities of elastic waves were calculated in different directions. When an elastic wave enters an anisotropic medium, it propagates as a longitudinal (P) wave and two transverse (S) waves. The two S-waves are polarized at right angles and propagate at different speeds. This is called shear wave splitting. The faster one will be called S_1 and the slower one S_2 . The S_1 velocities passing through single crystals of post-perovskite, perovskite and periclase, including their polarization, at conditions corresponding to Table 2, are shown in Fig. 5 in a spherical projection. The wave propagation pattern has to conform with crystal symmetry. We see that the maximum velocity difference in different directions

(anisotropy) is highest for periclase (Fig. 5d) and lowest for silicate perovskite (Fig. 5a). Post-perovskite based on Stackhouse et al. (2005) is more anisotropic (Fig. 5a) than for the Wentzcovitch et al. (2006) model (Fig. 5b), but the pattern is similar. In post-perovskite (Fig. 5a), a fast S_1 wave which propagates in the [001] crystal direction (center of figure) is relatively slow and polarized in the $[001] \times [010]$ plane. A fast S_1 wave propagating in the [100] direction is polarized in the $[100] \times [010]$ plane.

Knowing the single crystal elastic constants and local crystal orientation distribution, we can average to obtain local elastic properties along a streamline. There are different averaging schemes including Voigt (upper bound), Reuss (lower bound), geometric or arithmetic mean, or self-consistent averaging. Here we use the geometric mean (Matthies and Humbert, 1993) and a self-consistent method that takes grain shapes into account (Lebensohn et al., 2007). The latter is implemented in VPSC as a calculation independent of the visco-plastic formulation. For the case investigated here, with moderate single crystal anisotropy, results of the two averaging methods are very similar.

6. Results

With deformation mechanisms and elastic constants defined, we can now proceed to simulate the development of preferred orientation along streamline #189. For strain components we refer to Fig. 3. We assume that the aggregate is composed 25 vol.% of periclase and 75% of perovskite or post-perovskite. This corresponds approximately to a pyrolite composition of the mantle (e.g. Mattern et al., 2005; Ringwood, 1982). In our simulations we start with random orientation distributions of 1000 grains for each phase as the tracer enters the D'' zone (300 km above the CMB). Grain orientations and grain shapes

Table 1

Slip systems $\{hkl\}\langle uvw \rangle$ and critical resolved shear stress coefficients (crss) for various models. The crss are normalized so that the value for the softest system is 0.5 for MgO and 1.0 for perovskite and post-perovskite.

MgO	$\{111\}\langle 10\bar{1} \rangle$ 0.75	$\{110\}\langle \bar{1}10 \rangle$ 0.5	$\{100\}\langle 011 \rangle$ 1					
Perovskite	$(100)[010]$ 3	$(100)\langle 011 \rangle$ 4	$(010)[100]$ 3	$(010)\langle 101 \rangle$ 4	$(001)[100]$ 1	$(001)[010]$ 1	$(001)\langle 110 \rangle$ 1	
Postperovskite	$(100)[010]$	$(100)[001]$	$(010)[100]$	$(010)[001]$	$(001)[100]$	$(001)[010]$	$\{110\}\langle \bar{1}10 \rangle$	$\{110\}[001]$
A	1	1.5	3	3	3	3	3	2
B	3	3	1	1.5	3	3	3	4
C	2	2	4	4	1	1.5	3	4

Table 2
Density d (in g/cm^3) and stiffness coefficients C_{ij} (in GPa) of periclase (Karki et al., 2000), perovskite (Wentzovitch et al., 2004), post-perovskite 1 (Stackhouse et al., 2005) and post-perovskite 2 (Wentzovitch et al., 2006) at 125 GPa 3000 K.

	d	C_{11}	C_{12}	C_{13}	C_{22}	C_{23}	C_{33}	C_{44}	C_{55}	C_{66}
Periclase	5.07	1154.0	256.5	256.5	1154.0	256.5	1154.0	198.0	198.0	198.0
Perovskite	5.25	860.0	535.5	437.0	1067.5	467.5	1053.0	294.0	249.5	284.5
Post-perovskite 1	5.35	1220.0	474.0	359.0	899.0	493.0	1176.0	273.0	245.0	376.0
Post-perovskite 2	5.29	1104.5	454.6	429.0	869.5	504.3	1104.5	305.5	224.0	329.5

get updated at every step. As noted above, there are 6420 steps along streamline #189. In order to smooth statistical fluctuations we average over 6 steps. For simplicity (and for lack of information) we assume that crss remain constant (Table 1). Note that these are normalized crss and that the weakest slip system of MgO has a lower crss (0.5) than any of the other phases (1.0) (Karato, 1998b). It can thus be expected that a substantial amount of deformation concentrates on MgO, even though it is the minor phase. For the stress exponent (viscoplasticity), we assume a value of $n=3$ (e.g. Wu, 2002). Computing speed is not an issue (Kaminski and Ribe, 2004): on a PC with a 2.4 GHz processor computation of 6420 steps with a total of 2000 orientations takes less than half an hour.

In Appendix B (electronic supplement) we explore the effects of diffusion and note that both intracrystalline and grain boundary diffusion reduce texture development. In the lower mantle diffusion is clearly significant and thus we assume that only 50% of the strain is accommodated by slip and the rest by diffusion, resulting in a dislocation creep process. Also, we are not updating grain shapes once a grain has reached an aspect ratio of 3.0, although we allow for the ellipsoid to rotate rigidly inside the effective medium.

While the VPSC code keeps track of crystal orientation and deformation, it also records statistical information. Of particular interest is the activity of slip systems at each step, where activity is defined as the

relative contribution of each slip mode to the total shear. Details about slip system activities are displayed in Fig. 6. The sum of activities over all phases and slip systems is 1.0 at each step. For all models several systems are active at all times (on average more than 5, contributing more than 5% of the strain), though one dominates. On this plot we can see that a substantial amount of deformation is accommodated by the subordinate but weaker phase MgO (blue curves). Interestingly the system with the lowest crss, $\{110\}$ slip, is not the most active but rather $\{111\}$ slip. The reason is that more symmetrically equivalent slip planes/directions exist for $\{111\}\langle\bar{1}10\rangle$ (12) than for $\{110\}\langle\bar{1}10\rangle$ (6). For low symmetry crystals the softest system generally dominates. If we refer in the discussion to (001) slip we simply identify the dominant system, which does not exclude activity of others. Note that we have omitted the region around step #5600 in the plots of Fig. 6. It corresponds to the region with numerical instabilities (Fig. 3) but the influence on texture is negligible.

Texture evolution is a very dynamic process which is best illustrated with a movie (movie 2, supplementary material). It shows crystal rotations of (001) poles of 100 grains for post-perovskite C along streamline #189 with the CMB horizontal. Orientations rotate towards the texture maximum from both sides, supporting the conclusion that the strain path contains a pure shear (co-axial) component. In simple shear, rotations would be mainly with the shear sense, which is the case

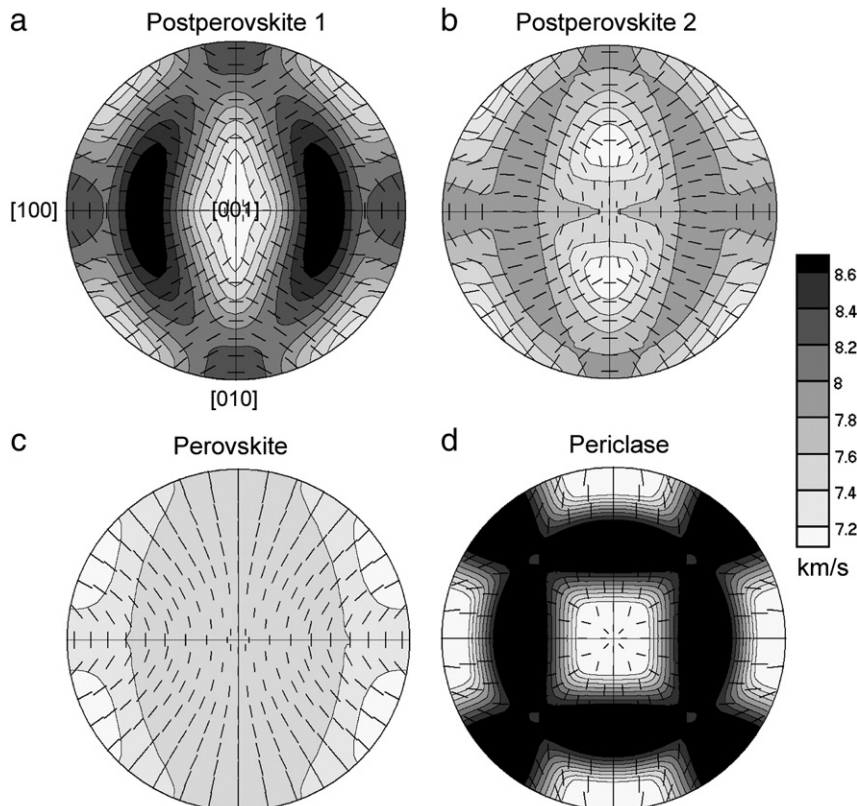


Fig. 5. Single crystal fast S-wave surfaces for (a) post-perovskite 1 (Stackhouse et al., 2005), (b) post-perovskite (Wentzovitch et al., 2006), (c) perovskite (Wentzovitch et al., 2004) and (d) periclase (Karki et al., 2000) at 125 GPa and 3000 K, corresponding to stiffness coefficients in Table 2. Lines indicate the polarization direction. Equal area projection.

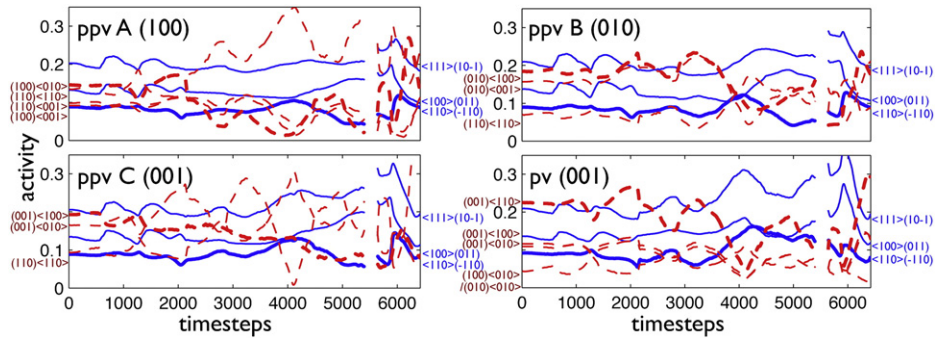


Fig. 6. Slip system activities for the four models. Blue (labels on right side) is MgO and red (labels on left side) is perovskite/post-perovskite. Slip systems with activity less than 0.1 are not plotted. The slip system with the lowest CRSS is plotted as bold line. There is a discontinuity around 5600 steps which is due to numerical instability. For slip systems also refer to Table 1.

in the final rotation with large shear components. Compare this for example with halite deformed in simple shear, where orientations rotate with variable speed in the sense of shear (Wenk et al., 2009).

The movie with discrete orientations best illustrates the “orientation distribution”. Obviously, the statement mentioned earlier “10% of the crystals are aligned” does not describe the actual case. In this movie each orientation has a different symbol size, which is proportional to the strain. More heavily deformed grains are concentrated in the main texture maximum at high angles to the CMB. If we were to apply a nucleation-based recrystallization model, these orientations would nucleate and grow, and dominate the texture. Thus the pattern would not change appreciably.

Fig. 7 illustrates a regular texture development along streamline #189 for post-perovskite C at some intervals shown on Fig. 2. Already at 900 steps, still in the subduction regime, (001) lattice planes orient preferentially and slightly asymmetrically parallel to the core–mantle boundary. The asymmetry is due to the component of simple shear (Fig. 3). This texture increases in strength but does not rotate during spreading. Only at the very end (6420 steps), during upwelling, is there a rapid 90° rotation and (001) planes become oriented perpendicular to the CMB.

Fig. 8 shows the pole figures at an intermediate position (3600 steps) for all models, i.e. post-perovskite A, B, C and perovskite. In each

case 25% periclase is included as a second phase. From the pole figures we see that for all models strong textures develop, but patterns are very different, as might be expected. For low symmetry crystals with few slip systems, we might intuitively guess that main slip planes reorient perpendicular to the compression direction and slip directions parallel to the extension direction. For the tracer, the compression direction is overall perpendicular to the CMB (Fig. 3, V_x/dx) and thus we have a (100) maximum for post-perovskite A with (100)-slip dominating, a (010) maximum for B with (010)-slip dominating, and a (001) maximum for C, with (001)-slip dominant. Cubic periclase has a more complex distribution with (110) poles normal to the CMB. The patterns are slightly asymmetric due to the component of simple shear.

Knowing orientation distributions and single crystal elastic properties (Table 2) we can estimate aggregate elastic properties by averaging over the orientation distribution and then, from stiffness tensors, calculate seismic wave velocities. Averaging of elastic constants was done with the geometric mean (Matthies and Humbert, 1993). Fig. 9 shows the S_1 and S_2 velocities ($S_1 > S_2$) and P-velocities corresponding to the textures in Fig. 8. For post-perovskite only the model with Stackhouse et al. (2005) single crystal properties is shown. In this spherical representation the CMB is horizontal. In the S_1 velocity figures the polarization direction of the fast S-wave is illustrated by lines that are parallel to the polarization. Anisotropy is

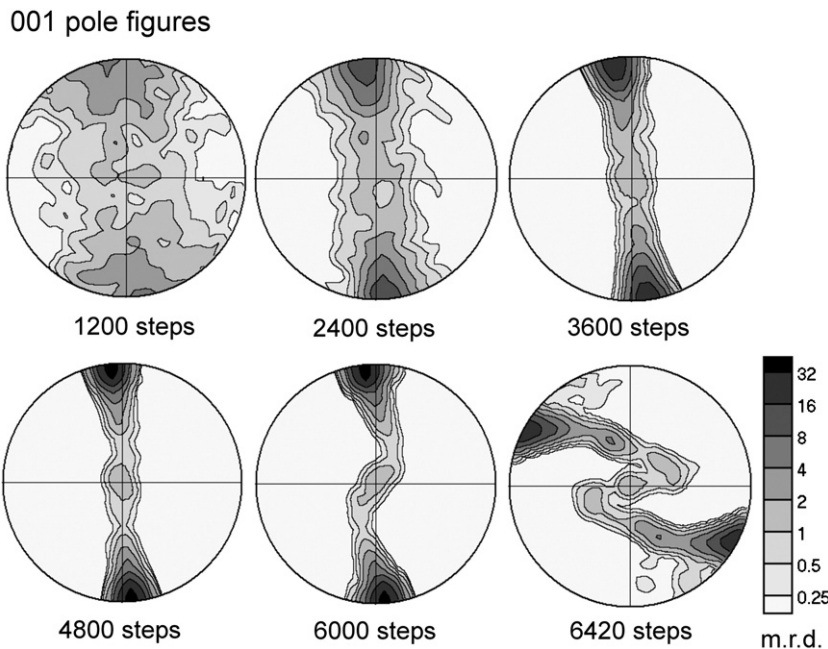


Fig. 7. 6 snapshots of (001) pole figures for post-perovskite C along streamline #189. Core–mantle boundary is horizontal. Equal area projection, logarithmic contour scale. Selected positions refer to circles in Fig. 2 (bottom).

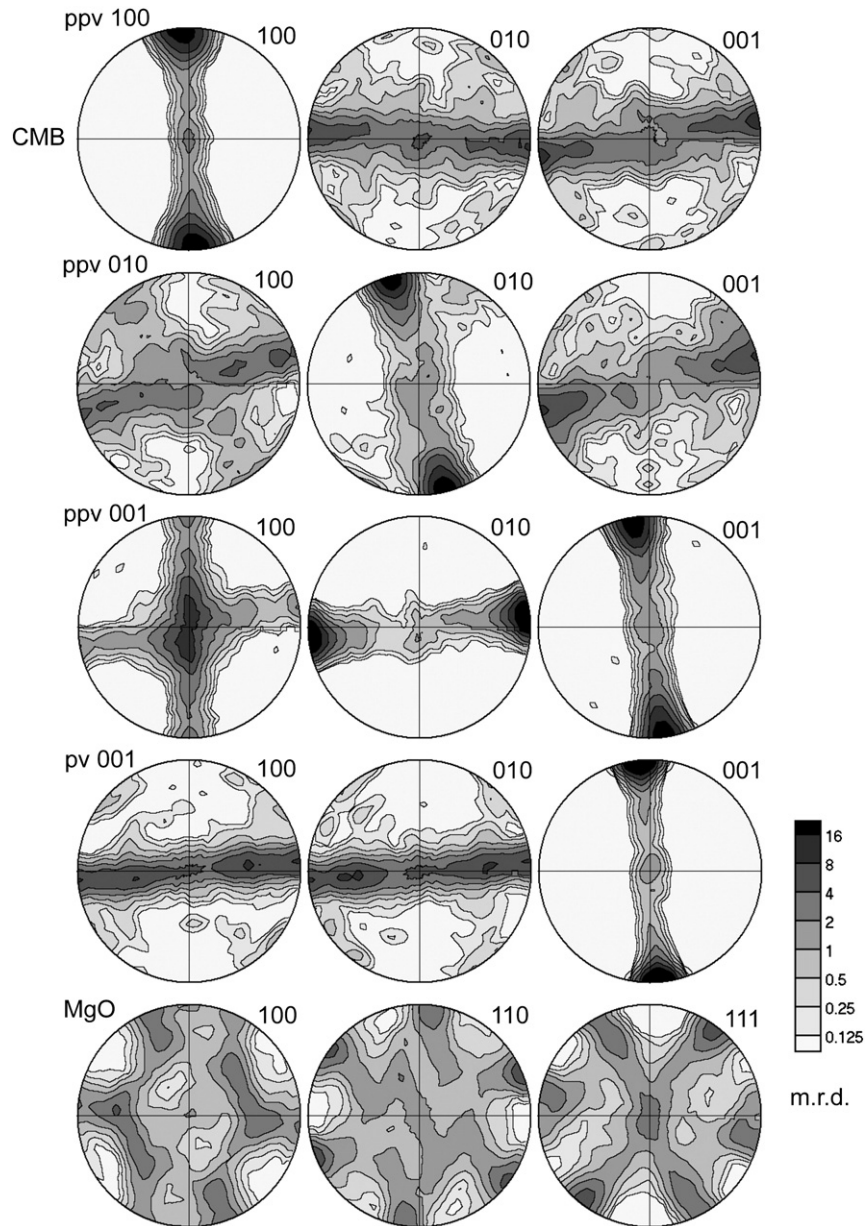


Fig. 8. Pole figures for post-perovskite (models A, B, and C), perovskite and magnesiowuestite after 3600 steps along streamline #189. Core–mantle boundary is horizontal (CMB). Equal area projection.

high if there is a large variation over the sphere. Shear wave splitting is high in a particular direction if corresponding S_1 and S_2 velocities are very different. For post-perovskite A and B fast S-waves are polarized parallel to the CMB, while for post-perovskite C and periclase they are polarized perpendicular to the CMB.

7. Discussion

As we described in the previous section, all four models for perovskite and post-perovskite predict strong preferred orientation patterns that develop rapidly during subduction. The patterns remain amazingly stable during spreading, increasing somewhat in strength. At the very end, they rotate 90° , during upwelling (Fig. 7). The three patterns of post-perovskite, each with some experimental support, are very different.

We are presenting here a 2-dimensional geodynamic model and thus macroscopic deformation is in plane strain, ranging from pure shear (coaxial) to simple shear (non-coaxial). In terms of texture development

this difference is significant. In pure shear rotations generally go towards certain concentrations which build up in strength, as in rolling of metals. In simple shear there is no such relationship (Bolmaro and Kocks, 1992; Canova et al., 1984). Rotations are overall in the sense of shear and texture maxima build up and attenuate as demonstrated for quartz (Wenk et al., 1989) and most recently for halite (Wenk et al., 2009). There is no evidence for the contentious assumption that “slip planes rotate into the shear plane and slip directions rotate into the shear direction”, though it is true for low symmetry crystals and low strain rate sensitivity (high n) that the dominant slip plane rotates slower when it is close to the shear plane. The case of tracer #189 is intermediate between pure shear and simple shear, as illustrated by Fig. 3 and also by the movie (movie 2, supplementary on-line material) where it is observed that rotations are from both sides towards the texture maximum, except at the very end.

At this point a brief discussion of the limitations of the simulations is in order. What is different between experiments, simulations and the lower mantle?

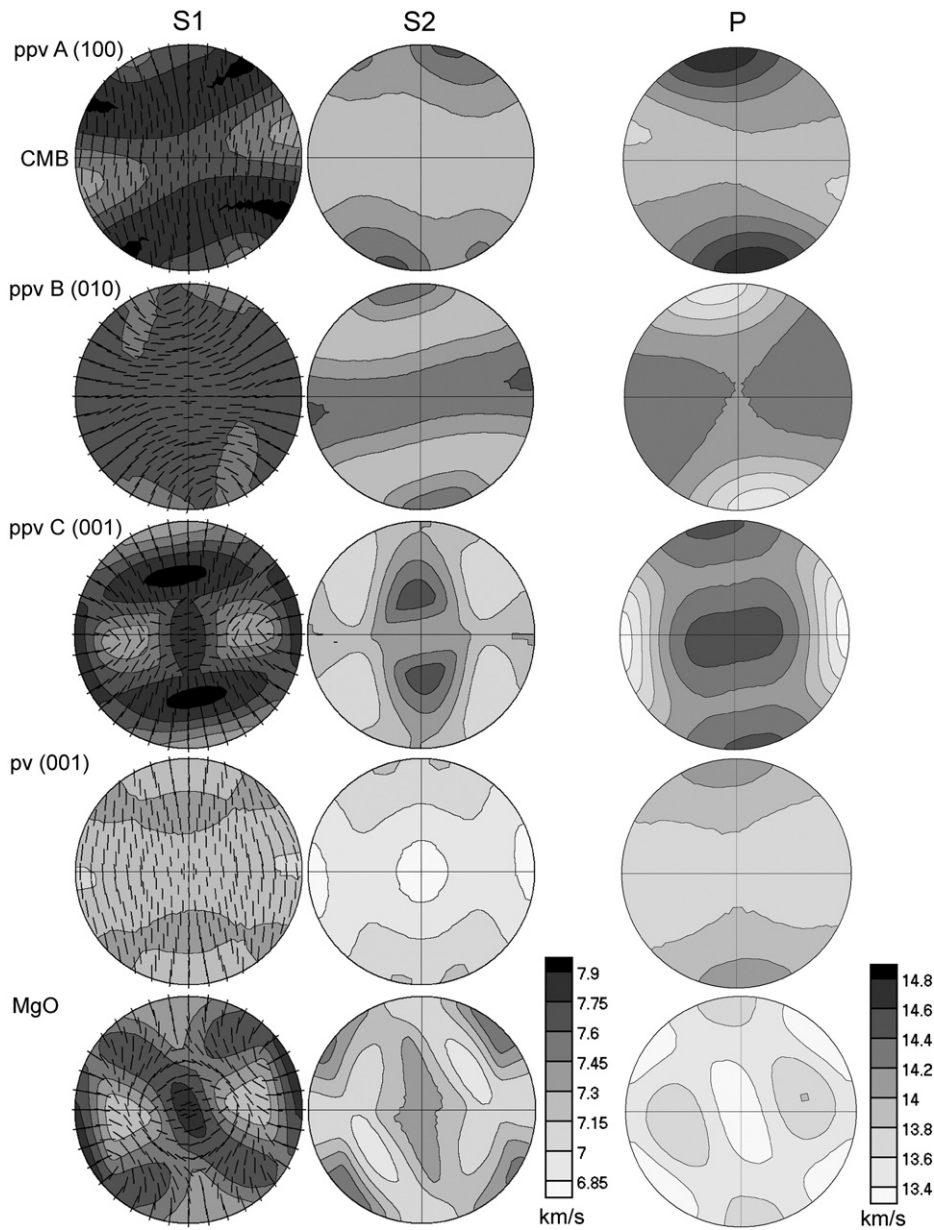


Fig. 9. Calculated S ($S_1 > S_2$)- and P-wave velocities corresponding to preferred orientation patterns shown in Fig. 8 (3600 steps) and single crystal elastic properties in Fig. 5. For post-perovskite only the average based on Stackhouse et al., 2005) is shown. Core–mantle boundary is horizontal (CMB). Equal area projection. Black lines indicate polarization of fast S-wave (S_1).

Below is a summary of parameters that have a profound effect on deformation mechanisms:

	Experiment	Mantle
Stress	High (slip and twinning)	Low (creep)
Temperature	Low(er) (slip and twinning)	High (creep, recrystallization)
Grain size	Small (grain boundary sliding)	Large (slip, climb, subgrains)
Strain	Medium (slip, twinning)	Large (slip, recrystallization)
Strain rate	High (slip and twinning)	Low (slip and creep)

The most profound differences, in our view, are stress and temperature. In many ways, it is expected that at high pressure and temperature in the lower mantle, mechanisms may be simpler than at low pressure and temperature, more like a hot-rolled metal than a crustal fault rock, and we can use analogies from metallurgy to extrapolate. At the low stress and high temperature, with a homologous temperature of 0.5 (see Appendix B, electronic supplement), we can exclude mechanical twinning as a mechanism. We did

take diffusion mechanisms into account by only accommodating 50% of the deformation by slip. This factor could be reduced and would result in slower (but still strong) texture development. We have mentioned earlier that recrystallization would probably not alter the pattern significantly. Clearly, there are uncertainties and we also should point out that the flow along streamline #189 is not representative of the whole lower mantle. It only illustrates one region with subduction and spreading, and, perhaps, upwelling into a large plume. As illustrated best by Fig. 2 (and movie 1), patterns as observed in the cell considered in this study are localized and not expected to prevail over large regions of the Earth as, for example convection patterns in the upper mantle. This is consistent with seismic observations that document anisotropy anomalies in only a few well-defined areas (Fig. 1).

Based on flow in the 2D geodynamic model both texture patterns (Fig. 8) as well as seismic anisotropies (Fig. 9) post-perovskite A, B and perovskite show a strong component of transverse isotropy. The polycrystal plasticity models for post-perovskite C and MgO show a

significant component of azimuthal anisotropy as can be seen in the variation in speed and splitting direction along the horizontal (CMB). Note that at the angles with reversed splitting direction, the magnitude of the splitting (difference between S_1 and S_2) is very small. It is difficult to constrain this component of anisotropy from seismic observations due to the scarce and localized seismic constraints and the simplification in our model of 2D plane strain input.

The absolute velocities (Fig. 9) for perovskite lie closest to the PREM values of ~ 7.2 km/s for S-waves and ~ 13.65 km/s for P-waves (Dziewonski and Anderson, 1981), whereas for post-perovskite, velocities for Stackhouse et al., 2005 are higher than PREM. Results for Wentzcovitch et al. (2006) lie closer to PREM. However, the velocities are not directly comparable, as first-principle calculations are for infinite frequency, while seismic frequencies are sensitive to physical dispersion due to anelasticity. Physical dispersion lowers the intrinsic velocity at lower frequencies. Additionally, the densities used in these calculations (from first principles) are also lower than PREM (resulting in higher velocities) and there is some uncertainty, especially since we assume pure Mg–Si–O phases and do not consider the influence of Fe-content or Ca-phases such as CaSiO_3 perovskite. Among other possibilities that need further exploration, lower PREM velocities could, for example, be caused by the occurrence of melt inclusions (Williams and Garnero, 1996).

A limitation of the VPSC model is that it assumes a homogeneous medium and microstructural features are not taken into account. This is particularly significant for polyphase materials with stiffer and weaker components. The model will favor weaker phases, even if they are subordinate. In reality weak minor phases may occur as inclusions in the

major phase or concentrate in triple junctions, forcing hard phases to accommodate most of the strain. Thus the dominance of slip activity by MgO ($\sim 50\%$) may be unrealistic. In some experiments of perovskite–periclase aggregates texture development of periclase was minimal (Wenk et al., 2004). This would need to be approached with finite element polycrystal plasticity models that can account for the topology of microstructures, but they are still unrealistic for such complex systems (e.g. Barton and Dawson, 2001; Mika and Dawson, 1999).

The same calculations as we did for streamline #189 were done for many locations along additional seven streamlines shown in Fig. 2 (bottom), obtaining texture patterns and seismic velocities for the whole area of the convection cell. In this case averaging of elastic properties was done with the self-consistent method in VPSC (Lebensohn et al., 2007). The elastic stiffness calculations were done for individual phases. Fig. 10 displays the interpolated fit of $\xi = (V_{SXH}^2/V_{SXV}^2)$ and (V_{PX}^2/V_{PZ}^2) . V_{SXH} is defined as the velocity of a diffracted S-wave traveling in the x-direction with a horizontal polarization and V_{SXV} as one with a vertical polarization (Fig. 2). V_{PX} is the velocity of a P-wave propagating in the x-direction and V_{PZ} is the P-wave velocity in the z-direction. This representation is comparable with Fig. 1, and although we do not impose general transverse isotropy, the azimuthal anisotropic components of the models are not plotted. Significant azimuthal anisotropy is present in the phases of post-perovskite C and MgO, mostly along the lowermost tracers close to the CMB, and for all phases within the upwelling.

For all models anisotropy increases with depth and progressive flow (x) and is largest near the CMB. This is due to an increase in strain, which is highest for the deep tracer 189. But, similar to Fig. 9,

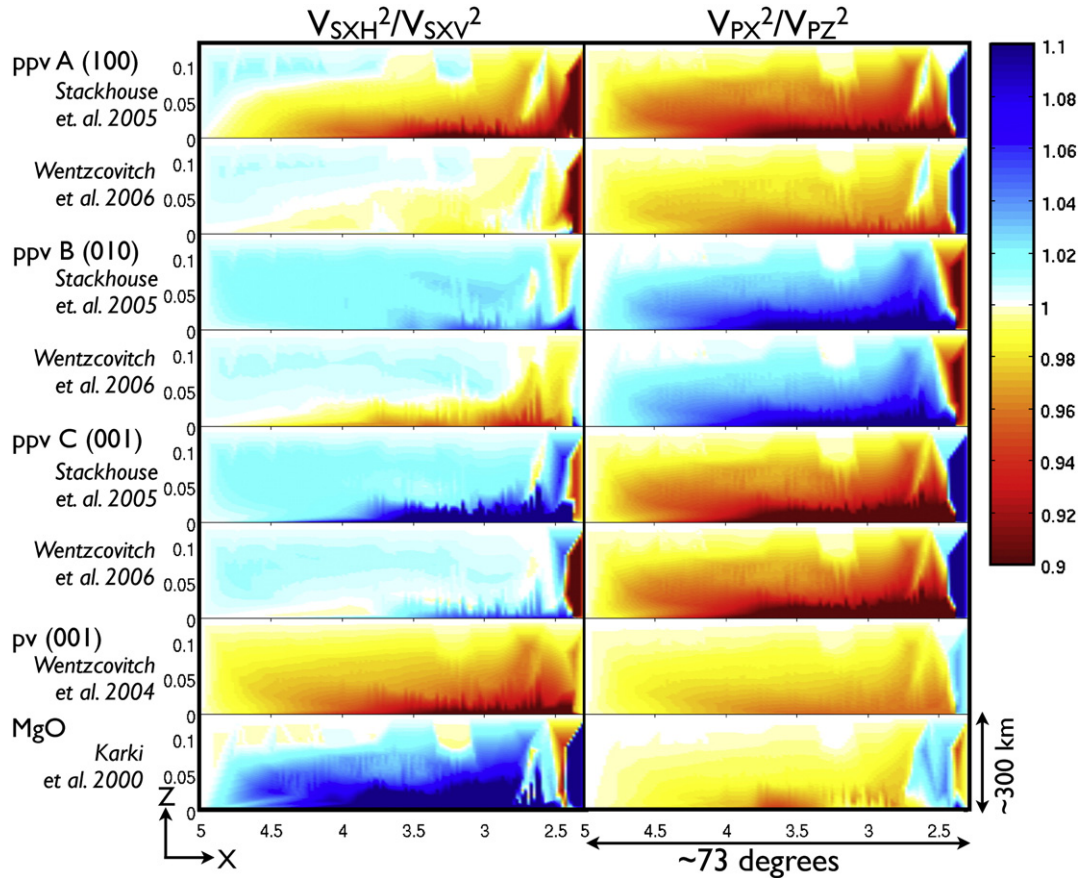


Fig. 10. Simulated S-wave and P-wave anisotropy for single phase models in D'' expressed by $\xi = (V_{SXH}^2/V_{SXV}^2)$ and (V_{PX}^2/V_{PZ}^2) for all seven models. V_{SXH} and V_{SXV} are the velocities of horizontally and vertically polarized wave traveling in the x-direction. Values less than 1.0 indicate that the fast S-wave is polarized parallel to the CMB. The ratio of the velocities of a P-wave traveling in the x-direction and a P-wave traveling in the vertical direction, quantifies the P-wave anisotropy. Values less than 1.0 indicate that the fast P-wave is parallel to the CMB. The behavior of the second phase periclase is the same for all models and only shown for the combination with perovskite. See text for definitions.

the different models show very different and distinct patterns: For perovskite (001), post-perovskite A (100) and to some extent for post-perovskite B (010), using [Wentzcvitch et al. \(2006\)](#) elasticity, fast S-waves are polarized perpendicular to the CMB (yellow/red colors – values less than 1.0). For all others they are polarized parallel to the CMB (blue colors – values greater than 1.0). S-wave anisotropy is strongest for post-perovskite C (001) and periclase, and weaker for post-perovskite B (010). The [Stackhouse et al. \(2005\)](#) elastic properties predict higher S-wave anisotropy than the [Wentzcvitch et al. \(2006\)](#) data.

Anisotropy of P-waves is represented as ($V_{P_x}^2/V_{P_z}^2$) in the right column of [Fig. 10](#). For P-waves the two elastic post-perovskite models produce similar results which are plausible since the main difference is in off-diagonal coefficients such as C_{13} which relate to S-waves. Except for post-perovskite B (blue colors – values greater than 1.0) vertical P waves are faster than horizontal ones (yellow/red colors – values less than 1.0). Furthermore for postperovskite A, postperovskite B and perovskite, P and S-wave anisotropies correlate, whereas for postperovskite C and MgO there is an anticorrelation.

Seismic studies show $V_{SH} > V_{SV}$ ($\xi > 1$) in fast regions, where (paleo)-slabs might be present (e.g. [Kustowski et al., 2008](#); [Panning and Romanowicz, 2006](#)) ([Fig. 1](#)) and thus a D'' layer with post-perovskite B and C would be most consistent. The anisotropy which is observed, e.g. in the Caribbean and under Alaska ($\xi_{max} = 1.04$, [Fig. 1](#)) is smaller than the predictions of the model ($\xi_{max} = 1.35$, $\xi_{mean} = 1.05$) which could be due to the underestimation of seismic anisotropy by averaging over long paths in the seismic data, especially in global models, or the overestimation of the amount of dislocation creep versus diffusion creep. The anticorrelation of P and S-wave anisotropies for postperovskite C and MgO also agrees with seismic observations mentioned before (e.g. [Beghein et al., 2006](#); [Tkalcic and Romanowicz, 2002](#); [Wyssession et al., 1999](#)).

The calculated patterns for S- and P-wave anisotropies reverse during upwelling ([Fig. 10](#), right side of diagrams). This is due to a rotation of textures caused by a rigid body rotation of the strain ellipse ([Fig. 2](#)). The texture rotation is evident in [Fig. 7](#) (6420 steps) as well as the very end of movie 2. Also this is consistent with seismic observation of $V_{SH} < V_{SV}$ in superplumes (e.g. [Kawai and Geller, 2010](#)). The reversal is not expressed for MgO which can be attributed to the cubic crystal symmetry and correspondingly complex pole-figures.

Thus, concluding from the characteristic anisotropy signature of the models, it appears that an aggregate of post-perovskite with dominant (001) slip (C) and periclase can best explain the observed seismic anisotropy in the D''. Note that this preferred model contains a component of azimuthal anisotropy close to the CMB. Perovskite and post-perovskite A and B produce patterns which are incompatible with seismic data.

This conclusion, based on macroscopic modeling, is also supported by recent mineral physics investigations of microscopic deformation mechanisms. It appears that $CaIrO_3$ with 010 slip (model B) ([Fig. 4b](#)) is a poor analog for $MgSiO_3$ as far as deformation mechanisms are concerned, because it has very different bonding characteristics ([Metsue et al., 2009](#)). The weak (100) texture in $MgSiO_3$ observed in some DAC experiments (model A, [Fig. 4a](#)) ([Merkel et al., 2007](#)) is likely due to the phase transformation, rather than ductile deformation and thus does not provide information on slip systems. New DAC experiments on $MgSiO_3$ ([Miyagi et al., 2010](#)) and $MgGeO_3$ ([Okada et al., 2010](#)) show clear evidence for texture strengthening by increasing pressure after the phase transformation, producing strong (001) textures ([Fig. 4c](#)) which can only be explained with dominant (001) slip ([Fig. 4h](#)).

There are other geodynamic models for D'' which rely on temperature and compositional variations and do not even require the presence of post-perovskite ([Hernlund and Tackley, 2007](#); [Hernlund et al., 2005](#)). Such models can explain the anomalously

low velocity layer but fail to account for the characteristic S-wave polarization. Another possibility is the role of shape preferred orientation (SPO) in these regions ([Lay et al., 1998b](#)), including features like layered structures ([Kendall and Silver, 1996](#)) or regions of partial melt ([Williams and Garnero, 1996](#)). Concerning SPO, neither post-perovskite nor magnesiowuestite are intrinsically needles or platelets and only attain a shape through deformation by dislocation glide and their shape is thus directly linked to texture.

We do not consider our study to contain the last word on D'' anisotropy structure. Many uncertainties remain. On the geodynamic side more realistic 3D models need to be developed that include slab subduction and broad plume upwelling. In 3D models, strain may be partitioned differently as material from tabular slabs is swept into more-cylindrical upwelling regions. Furthermore, the LLSVPs likely exhibit compositional heterogeneity that may cause more complex deformation as slabs approach them (e.g. [Lassak et al., 2010](#)). In mineral physics it is important to better characterize post-perovskite deformation mechanisms, particularly variations with temperature. We have mentioned the complications of polyphase on plasticity. Experiments are needed to define the topology of microstructures and models may need to be refined. Also, the influence of composition such as Mg–Fe should be further investigated, both concerning elastic properties and slip systems. It is fairly well-known for magnesiowuestite ([Antoangeli et al., 2011](#); [Lin et al., 2009](#); [Tommaseo et al., 2006](#); [Yamazaki and Karato, 2002](#)) but much less for perovskite and post-perovskite. This requires delicate DAC experiments and first principles calculations. On the seismology side, it would be extremely useful to have data to constrain the 3D elastic structure in the deep Earth. A natural next step is to perform forward calculations that investigate how seismic waves are affected by passing through a hypothetical D'' as illustrated in [Fig. 10](#).

8. Conclusions

At large strains, as one can surely expect in the D'' zone, it is very likely that strong preferred orientation develops, even if dislocation glide is combined with considerable diffusion. The project taught us that microscopic mechanisms can be inferred from DAC and D-DIA experiments, but there are limitations. Caution is required with analogs. Conditions may be different in experiments, particularly where phase transformations at high stress can falsify patterns. In the end, comparison of models with macroscopic seismic observations has been most useful in constraining microscopic deformation mechanisms. It seems that the latest experiments on $MgSiO_3$ post-perovskite ([Miyagi et al., 2010](#)) are in good agreement and thus dominant (001) slip in post-perovskite combined with {110} and {111} slip in magnesiowuestite best explains the seismic observations, i.e. high anisotropy and polarization of fast S-waves parallel to the CMB in zones of spreading, as well as anti-correlation between P and S-wave anisotropies.

Supplementary materials related to this article can be found online at [doi:10.1016/j.epsl.2011.03.021](https://doi.org/10.1016/j.epsl.2011.03.021).

Acknowledgments

This work was supported by NSF grants EAR-0757608 and EAR-0456356 from the CSEDI program as well as EAR-0836402 and CDAC. Discussions with Lowell Miyagi, Stephen Stackhouse and Waruntorn Kanitpanyacharoen are gratefully acknowledged. We are appreciative for constructive reviews that helped us to improve the manuscript.

References

- Ammann, M.W., Brodholt, J.P., Wookey, J., Dobson, D.P., 2010. First-principles constraints on diffusion in lower-mantle minerals and a weak D'' layer. *Nature* 465, 462–465. [doi:10.1038/nature09052](https://doi.org/10.1038/nature09052).

- Antoangeli, D., Siebert, J., Aracne, C.M., Farber, D.L., Bosak, A., Hoesch, M., Krisch, M., Ryerson, F.J., Fiquet, G., Badro, J., 2011. Spin crossover in ferropericlase at high pressure: a seismological transparent transition? *Science* 331, 64–67. doi:10.1126/science.1198429.
- Barton, N.R., Dawson, P.R., 2001. On the spatial arrangement of lattice orientations in hot-rolled multiphase titanium. *Modell. Simul. Eng.* 9, 433–463.
- Becker, T.W., Kustowski, B., Ekström, G., 2008. Radial seismic anisotropy as a constraint for upper mantle rheology. *EPSL* 267, 213–227. doi:10.1016/j.epsl.2007.11.038.
- Beghein, C., Trampert, J., Van Heijst, H.J., 2006. Radial anisotropy in seismic reference models of the mantle. *J. Geophys. Res.* 11, B02303. doi:10.1029/2005JB003728.
- Blackman, D.K., Wenk, H.-R., Kendall, J.M., 2002. Seismic anisotropy in the upper mantle: factors that affect mineral texture and effective elastic properties. *Geochem. Geophys. Geosyst.* 3, 8601. doi:10.1029/2001GC000248.
- Bolmaro, R.E., Kocks, U.F., 1992. A comparison of the texture development in pure and simple shear and during path changes. *Scr. Metall. Mater.* 27, 1717–1722. doi:10.1016/0956-716X(92)90008-3.
- Buffett, B.A., Wenk, H.-R., 2001. Texturing of the Earth's inner core by Maxwell stresses. *Nature* 413, 60–63. doi:10.1038/35092543.
- Bullen, K.E., 1950. An earth model based on a compressibility–pressure hypothesis. *Geophys. J. Int.* 6, 50–59. doi:10.1111/j.1365-246X.1950.tb02973.x.
- Canova, G.R., Kocks, U.F., Jonas, J.J., 1984. Theory of torsion texture development. *Acta Metall.* 32, 211–226. doi:10.1016/0001-6160(84)90050-6.
- Carrez, P., Ferré, D., Cordier, P., 2007. Implications for plastic flow in the deep mantle from modelling dislocations in MgSiO₃ minerals. *Nature* 446, 68–70. doi:10.1038/nature03593.
- Chen, J., Weidner, D.J., Vaughan, M.T., 2002. The strength of Mg_{0.9}Fe_{0.1}SiO₃ perovskite at high pressure and temperature. *Nature* 419, 824–826. doi:10.1038/nature01130.
- Dawson, P.R., Wenk, H.-R., 2000. Texturing of the upper mantle during convection. *Philos. Mag.* A 80, 573–598. doi:10.1080/01418610008212069.
- Dziewonski, A.M., Anderson, D.L., 1981. Preliminary reference Earth model. *Phys. Earth Plan. Int.* 25, 297–356. doi:10.1016/0031-9201(81)90046-7.
- Garnero, E., Revenaugh, J., Lay, T., Kellogg, L., 1998. Ultra low velocity zones at the core–mantle boundary. In: Gurnis, M., et al. (Ed.), “The Core–Mantle Boundary Region”. : Geodynamics Monograph, 28. American Geophysical Union, Washington D.C., pp. 319–334.
- Garnero, E.J., Maupin, V., Lay, T., Fouch, M.J., 2004. Variable azimuthal anisotropy in Earth's lowermost mantle. *Science* 306, 259–261. doi:10.1126/science.1103411.
- Heidelbach, F., Stretton, I., Langenhorst, F., Mackwell, S., 2003. Fabric evolution during high shear strain deformation of magnesiowüstite (Mg_{0.8}Fe_{0.2}O). *J. Geophys. Res.* 108, 2154.
- Helmlinger, D., Lay, T., Ni, S., Gurnis, M., 2005. Deep mantle structure and the post-perovskite phase transition. *PNAS* 102, 17257–17263. doi:10.1073/pnas.0502504102.
- Hernlund, J.W., Tackley, P.J., 2007. Some dynamical consequences of partial melting in Earth's deep mantle. *Phys. Earth Plan. Int.* 162, 149–163. doi:10.1016/j.pepi.2007.04.005.
- Hernlund, J.W., Thomas, C., Tackley, P.J., 2005. A doubling of the post-perovskite phase boundary and structure of the Earth's lowermost mantle. *Nature* 434, 882–886. doi:10.1038/nature03472.
- Hobbs, B.E., Heard, H.C. (Eds.), 1986. *Laboratory Studies, in Mineral and Rock Deformation*. : Monograph, 36. American Geophysical Union, Washington D.C.
- Houser, C., 2007. Constraints on the presence or absence of post-perovskite in the lowermost mantle from long-period seismology. In: Hirose, K., et al. (Ed.), “Post-Perovskite: the Last Mantle Phase Transition”. Monograph, 174. American Geophysical Union, Washington D.C., pp. 191–216.
- Hunt, S.A., Weidner, D.J., Li, L., Wang, L., Walte, N.P., Brodholt, J.P., Dobson, D.P., 2009. Weakening of calcium iridate during its transformation from perovskite to post-perovskite. *Nat. Geosci.* 2, 794–797. doi:10.1038/ngeo663.
- Kaminski, E., Ribe, N.M., 2004. D–rex, a program for calculation of seismic anisotropy due to crystal lattice preferred orientation in the convective upper mantle. *Geophys. J. Int.* 158, 744–752. doi:10.1111/j.1365-246X.2004.02308.x.
- Karato, S., 1998a. Some remarks on the origin of seismic anisotropy in the D" layer. *Earth Planets Space* 50, 1019–1028.
- Karato, S.I., 1998b. Seismic anisotropy in the deep mantle, boundary layers and the geometry of mantle convection. *Pure Appl. Geophys.* 151, 565–587. doi:10.1007/s000240050130.
- Karki, B.B., Wentzcovitch, R.M., De Gironcoli, S., Baroni, S., 2000. High-pressure lattice dynamics and thermoelasticity of MgO. *Phys. Rev. B* 61, 8793–8800. doi:10.1103/PhysRevB.61.8793.
- Kawai, K., Geller, R.J., 2010. The vertical flow in the lowermost mantle beneath the Pacific form inversion of seismic waveforms for anisotropic structure. *EPSL* 297, 190–197. doi:10.1016/j.epsl.2010.05.037.
- Kendall, J.M., 2000. Seismic anisotropy in the boundary layers of the mantle. In: Karato, S., et al. (Ed.), “Earth's Deep Interior: Mineral Physics and Tomography from the Atomic to the Global Scale”. : Monograph, 117. American Geophysical Union, Washington D.C., pp. 133–159.
- Kendall, J.M., Silver, P.G., 1996. Constraints from seismic anisotropy on the nature of the lowermost mantle. *Nature* 381, 409–412. doi:10.1038/381409a0.
- Kustowski, B., Ekström, G., Dziewonski, A.M., 2008. Anisotropic shear-wave velocity structure of the Earth's mantle: a global model. *J. Geophys. Res.* 113, B06306. doi:10.1029/2007JB005169.
- Lassak, T.M., McNamara, A.K., Zhong, S., 2007. Influence of thermochemical piles on topography at Earth's core–mantle boundary. *EPSL* 261, 443–455. doi:10.1016/j.epsl.2007.07.015.
- Lassak, T.M., McNamara, A.K., Garnero, E.J., Zhong, S., 2010. Core–mantle boundary topography as a possible constraint on lower mantle chemistry and dynamics. *EPSL* 289, 232–241. doi:10.1016/j.epsl.2009.11.012.
- Lay, T., 2008. Sharpness of the D" discontinuity beneath the Cocos Plate: implications for the perovskite to post-perovskite phase transition. *Geophys. Res. Lett.* 35, (L03304), 1–5. doi:10.1029/2007GL032465.
- Lay, T., Helmlinger, D.V., 1983. A shear velocity discontinuity in the lower mantle. *Geophys. Res. Lett.* 10, 63–66. doi:10.1029/GL010i001p00063.
- Lay, T., Williams, Q., Garnero, E.J., 1998a. The core–mantle boundary layer and deep Earth dynamics. *Nature* 392, 461–468. doi:10.1038/33083.
- Lay, T., Williams, Q., Garnero, E.J., Kellogg, L., Wyssession, M.E., 1998b. Seismic wave anisotropy in the D" region and its implications. In: Gurnis, M., et al. (Ed.), “The Core–Mantle Boundary Region”. : Geodynamics Monograph, 28. American Geophysical Union, Washington D.C., pp. 299–318.
- Lebensohn, R.A., Tomé, C.N., 1993. A self-consistent anisotropic approach for the simulation of plastic deformation and texture development of polycrystals: application to zirconium alloys. *Acta Metall. Mater.* 41, 2611–2624. doi:10.1016/0956-7151(93)90130-K.
- Lebensohn, R.A., Tomé, C.N., Castaneda, P.P., 2007. Self-consistent modelling of the mechanical behaviour of viscoplastic polycrystals incorporating intragranular field fluctuations. *Philos. Mag.* 87, 4287–4322. doi:10.1080/14786430701432619.
- Lin, J.F., Struzhkin, V.V., Jacobsen, S.D., Hu, M.Y., Chow, P., Kung, J., Liu, H., Mao, H.-K., Hemley, R.J., 2005. Spin transition of iron in magnesiowüstite in the Earth's lower mantle. *Nature* 436, 377–380. doi:10.1038/nature03825.
- Lin, J.F., Wenk, H.-R., Voltolini, M., Speziale, S., Shu, J., Duffy, T.S., 2009. Deformation of lower-mantle ferropericlase (Mg, Fe) O across the electronic spin transition. *Phys. Chem. Min.* 36, 585–592.
- Lithgow-Bertelloni, C., Gurnis, M., 1997. Cenozoic subsidence and uplift of continents from time-varying dynamic topography. *Geology* 25, 735–738. doi:10.1130/0091-7613.
- Long, M.D., 2009. Complex anisotropy in D" beneath the eastern Pacific from SKS–SKKS splitting discrepancies. *EPSL* 283, 181–189. doi:10.1016/j.epsl.2009.04.019.
- Masters, G., Laske, G., Bolton, H., Dziewonski, A.M., 2000. The relative behavior of shear velocity, bulk sound speed, and compressional velocity in the mantle: implications for chemical and thermal structure. In: Karato, S., et al. (Ed.), “Earth's Deep Interior: Mineral Physics and Tomography from the Atomic to the Global Scale”. : Monograph, 117. American Geophysical Union, Washington D.C., pp. 63–87.
- Mattern, E., Matas, J., Ricard, Y., Bass, J., 2005. Lower mantle composition and temperature from mineral physics and thermodynamic modelling. *Geophys. J. Int.* 160, 973–990. doi:10.1111/j.1365-246X.2004.02549.x.
- Matthies, S., Humbert, M., 1993. The realization of the concept of a geometric mean for calculating physical constants of polycrystalline materials. *Phys. Status Solidi* 177, K47–K50.
- Maupin, V., 1994. On the possibility of anisotropy in the D" layer as inferred from the polarization of diffracted S waves. *Phys. Earth Plan. Int.* 87, 1–32. doi:10.1016/0031-9201(94)90019-1.
- Maupin, V., Garnero, E.J., Lay, T., Fouch, M.J., 2005. Azimuthal anisotropy in the D" layer beneath the Caribbean. *J. Geophys. Res.* 110, B08301. doi:10.1029/2004JB003506.
- McNamara, A.K., van Keken, P.E., Karato, S.I., 2002. Development of anisotropic structure in the Earth's lower mantle by solid-state convection. *Nature* 416, 310–314. doi:10.1038/416310a.
- McNamara, A.K., van Keken, P.E., Karato, S.I., 2003. Development of finite strain in the convecting lower mantle and its implications for seismic anisotropy. *J. Geophys. Res.* 108 (B5), 2230. doi:10.1029/2002JB001970.
- Merkel, S., Wenk, H.-R., Shu, J., Shen, G., Gillet, P., Mao, H., Hemley, R.J., 2002. Deformation of polycrystalline MgO at pressures of the lower mantle. *J. Geophys. Res.* 107, 2271. doi:10.1029/2001JB000920.
- Merkel, S., McNamara, A.K., Kubo, A., Speziale, S., Miyagi, L., Meng, Y., Duffy, T.S., Wenk, H.-R., 2007. Deformation of (Mg, Fe) SiO₃ post-perovskite and D" anisotropy. *Science* 316, 1729–1732. doi:10.1126/science.1140609.
- Metsue, A., Carrez, P., Mainprice, D., Cordier, P., 2009. Numerical modelling of dislocations and deformation mechanisms in CaIrO₃ and MgGeO₃ post-perovskites—comparison with MgSiO₃ post-perovskite. *Phys. Earth Planet. Inter.* 174, 165–173. doi:10.1016/j.pepi.2008.04.003.
- Miika, D.P., Dawson, P.R., 1999. Polycrystal plasticity modeling of intracrystalline boundary textures. *Acta Mater.* 47, 1355–1369. doi:10.1016/S1359-6454(98)00386-3.
- Miyagi, L., Nishiyama, N., Wang, Y., Kubo, A., West, D.V., Cava, R.J., Duffy, T.S., Wenk, H.-R., 2008. Deformation and texture development in CaIrO₃ post-perovskite phase up to 6 GPa and 1300 K. *EPSL* 268, 515–525. doi:10.1016/j.epsl.2008.02.005.
- Miyagi, L., Kanitpanyacharoen, W., Kaercher, P., Lee, K.K.M., Wenk, H.R., 2010. Slip systems in MgSiO₃ post-perovskite: implications for D" anisotropy. *Science* 329, 1639–1641. doi:10.1126/science.1192465.
- Miyajima, N., Walte, N., 2009. Burgers vector determination in deformed perovskite and post-perovskite of CaIrO₃ using thickness fringes in weak-beam dark-field images. *Ultramicroscopy* 109, 683–692. doi:10.1016/j.ultramic.2009.01.010.
- Molinari, A., Canova, G.R., Ahzi, S., 1987. A self-consistent approach of the large deformation polycrystal viscoplasticity. *Acta Metall.* 35, 2983–2994. doi:10.1016/0001-6160(87)90297-5.
- Moresi, L., Gurnis, M., 1996. Constraints on the lateral strength of slabs from three-dimensional dynamic flow models. *EPSL* 138, 15–28. doi:10.1016/0012-821X(95)00221-W.
- Ni, S., Tan, E., Gurnis, M., Helmlinger, D., 2002. Sharp sides to the African superplume. *Science* 296, 1850–1852. doi:10.1126/science.1070698.
- Nowacki, A., Wookey, J., Kendall, J.-M., 2010. Deformation of the lowermost mantle from seismic anisotropy. *Nature* 467, 1091–1094. doi:10.1038/nature09507.
- Okada, T., Yagi, T., Niwa, K., Kikigawa, T., 2010. Lattice-preferred orientations in post-perovskite-type MgGeO₃ formed by transformations from different pre-phases. *Phys. Earth Plan. Int.* 180, 195–202. doi:10.1016/j.pepi.2009.08.002.

- Panning, M., Romanowicz, B., 2006. A three-dimensional radially anisotropic model of shear velocity in the whole mantle. *Geophys. J. Int.* 167, 361–379. doi:10.1111/j.1365-246X.2006.03100.x.
- Paterson, M.S., Olgaard, D.L., 2000. Rock deformation tests to large shear strains in torsion. *J. Struct. Geol.* 22, 1341–1358. doi:10.1016/S0191-8141(00)00042-0.
- Pfaff, F., 1859. Versuche über den Einfluss des Drucks auf die optischen Eigenschaften doppeltbrechender Krystalle. *Ann. Phys.* 183, 333–338.
- Poirier, J.P., Beauchesne, S., Guyot, F., 1991. Deformation mechanisms of crystals with perovskite structure. In: Navrotsky, A., Weidner, D. (Eds.), "Perovskite: A Structure of Great Interest to Geophysics and Materials Science". : Geophysical Monograph, 45. Am. Geophys. U, Washington D.C, pp. 119–123.
- Ringwood, A.E., 1982. Phase transformations and differentiation in subducted lithosphere: implications for mantle dynamics basalt petrogenesis and crustal evolution. *J. Geol.* 90, 611–642. doi:10.1086/628721.
- Stackhouse, S., Brodholt, J.P., 2007. The high-temperature elasticity of MgSiO₃ post-perovskite. In: Hirose, K. (Ed.), "Post-perovskite: The Last Mantle Phase Transition". : Monograph, 174. American Geophysical Union, Washington D.C, pp. 99–128.
- Stackhouse, S., Brodholt, J.P., 2008. Elastic properties of the post-perovskite phase of Fe₂O₃ and implications for ultra-low velocity zones. *Phys. Earth Planet. Inter.* 170, 260–266. doi:10.1016/j.pepi.2008.07.010.
- Stackhouse, S., Brodholt, J.P., Wookey, J., Kendall, J.M., Price, G.D., 2005. The effect of temperature on the seismic anisotropy of the perovskite and post-perovskite polymorphs of MgSiO₃. *EPSL* 230, 1–10. doi:10.1016/j.epsl.2004.11.021.
- Su, W., Dziewonski, A.M., 1997. Simultaneous inversion for 3-D variations in shear and bulk velocity in the mantle. *Phys. Earth Plan. Int.* 100, 135–156. doi:10.1016/S0031-9201(96)03236-0.
- Tkalcic, H., Romanowicz, B., 2002. Short scale heterogeneity in the lowermost mantle: insights from PcP-P and ScS-S data. *EPSL* 201, 57–68. doi:10.1016/S0012-821X(02)00657-X.
- To, A., Romanowicz, B., Capdeville, Y., Takeuchi, N., 2005. 3D effects of sharp boundaries at the borders of the African and Pacific superplumes: observation and modeling. *EPSL* 233, 137–153. doi:10.1016/j.epsl.2005.01.037.
- Tommaseo, C.E., Devine, J., Merkel, S., Speziale, S., Wenk, H.-R., 2006. Texture development and elastic stresses in magnesio-wüstite at high pressure. *Phys. Chem. Min.* 33, 84–97. doi:10.1007/s00269-005-0054-x.
- Vinnik, L., Farra, V., Romanowicz, B., 1989. Observational evidence for diffracted SV in the shadow of the Earth's core. *Geophys. Res. Lett.* 16, 519–522. doi:10.1029/GL016i006p00519.
- Wang, Y., Durham, W.B., Getting, I.C., Weidner, D.J., 2003. The deformation-DIA: a new apparatus for high temperature triaxial deformation to pressures up to 15 GPa. *Rev. Sci. Instrum.* 74, 3002–3011. doi:10.1063/1.1570948.
- Wenk, H.-R., Canova, G., Molinari, A., Kocks, U.F., 1989. Viscoplastic modeling of texture development in quartzite. *J. Geophys. Res.* 94, 17895–17906. doi:10.1029/JB094iB12p17895.
- Wenk, H.-R., Baumgardner, J.R., Lenzensohn, R.A., Tomé, C.N., 2000. A convection model to explain anisotropy in the inner core. *J. Geophys. Res.* 105, 5663–5677. doi:10.1029/1999JB900346.
- Wenk, H.-R., Lonardelli, I., Pehl, J., Devine, J., Prakapenka, V., Shen, G., Mao, H.-K., 2004. In situ observation of texture development in olivine, ringwoodite, magnesio-wüstite and silicate perovskite at high pressure. *EPSL* 226, 507–519. doi:10.1016/j.epsl.2004.07.033.
- Wenk, H.-R., Lonardelli, I., Merkel, S., Miyagi, L., Pehl, J., Speziale, S., Tommaseo, C.E., 2006a. Deformation textures produced in diamond anvil experiments, analysed in radial diffraction geometry. *J. Phys. Condens. Matter* 18, S933. doi:10.1088/0953-8984/18/25/S02.
- Wenk, H.-R., Speziale, S., McNamara, A.K., Garnero, E.J., 2006b. Modeling lower mantle anisotropy development in a subducting slab. *EPSL* 245, 302–314. doi:10.1016/j.epsl.2006.02.028.
- Wenk, H.-R., Armann, M., Burlini, L., Kunze, K., Bortolotti, M., 2009. Large strain shearing of halite: experimental and theoretical evidence for dynamic texture changes. *EPSL* 280, 205–210. doi:10.1016/j.epsl.2009.01.036.
- Wentzovitch, R.M., Stixrude, L., 2010. Theoretical and computational methods in mineral physics. *Geophysical Applications. : Reviews in Mineralogy & Geochemistry*, 71. Mineral. Soc. America, Washington D.C.
- Wentzovitch, R.M., Karki, B.B., Cococcioni, M., De Gironcoli, S., 2004. Thermoelastic properties of MgSiO₃-perovskite: insights on the nature of the Earth's lower mantle. *Phys. Rev. Lett.* 92, 18501–18505. doi:10.1103/PhysRevLett.92.018501.
- Wentzovitch, R.M., Tsuchiya, T., Tsuchiya, J., 2006. MgSiO₃ post-perovskite at D" conditions. *PNAS* 103, 543–546. doi:10.1073/pnas.0506879103.
- Wentzovitch, R.M., Wu, Z., Carrier, P., 2010. In: Wentzovitch, R.M., Stixrude, L. (Eds.), "First principles quasiharmonic thermoelasticity of mantle minerals": *Reviews in Mineralogy & Geochemistry*, 71, pp. 99–128. doi:10.2138/rmg.2010.71.5.
- Williams, Q., Garnero, E.J., 1996. Seismic evidence for partial melt at the base of Earth's mantle. *Science* 273, 1528–1530. doi:10.1126/science.273.5281.1528.
- Wookey, J., Kendall, J.M., 2007. Seismic anisotropy of post-perovskite and the lowermost mantle. In: Hirose, K., et al. (Ed.), "Post-perovskite: The Last Mantle Phase Transition". : Monograph, 174. American Geophysical Union, Washington D.C, pp. 171–190.
- Wookey, J., Kendall, J.M., 2008. Constraints on lowermost mantle mineralogy and fabric beneath Siberia from seismic anisotropy. *EPSL* 275, 32–42. doi:10.1016/j.epsl.2008.07.049.
- Wu, P., 2002. Effects of mantle flow law stress exponent on postglacial induced surface motion and gravity in Laurentia. *Geophys. J. Int.* 148, 676–686. doi:10.1046/j.1365-246X.2002.01620.x.
- Wyssession, M., Lay, T., Revenaugh, J., Williams, Q., Garnero, E.J., Jeanloz, R., Kellogg, L., 1998. The D" discontinuity and its implications. In: Gurnis, M., et al. (Ed.), "The Core-Mantle Boundary Region". *Geodynamics Monograph*, 28. American Geophysical Union, Washington D.C, pp. 273–298.
- Wyssession, M.E., Langenhorst, A., Fouch, M.J., Fischer, K.M., Al-Eqabi, G.I., Shore, P.J., Clarke, T.J., 1999. Lateral variations in compressional/shear velocities at the base of the mantle. *Science* 284, 120–125. doi:10.1126/science.284.5411.120.
- Yamazaki, D., Karato, S.-I., 2002. Fabric development in (Mg, Fe)O during large strain, shear deformation: implications for seismic anisotropy in Earth's lower mantle. *Phys. Earth Plan. Int.* 131, 251–267. doi:10.1016/S0031-9201(02)00037-7.